Interfacial Bonding Stabilizes Rhodium and Rhodium Oxide Nanoparticles on Layered Nb Oxide and Ta Oxide Supports

Megan E. Strayer,[†] Jason M. Binz,[‡] Mihaela Tanase,[§,‖] Seyed Mehdi Kamali Shahri,[‡] Renu Sharma,[§] Robert M. Rioux,*[,‡] and Thomas E. Mallouk*[,†]

[†]Department of Chemistry and [‡]Department of Chemical Engineering, The Pennsylvania State University, University Park, Pennsylvania 16802, United States
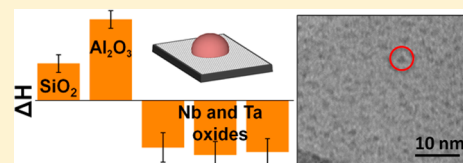
[§]Center for Nanoscale Science and Technology, National Institute of Science and Technology, Gaithersburg, Maryland 20899, United States

[‖]Institute for Research in Electronics and Applied Physics, University of Maryland, College Park, Maryland 20742-3511, United States

S *Supporting Information*

ABSTRACT: Metal nanoparticles are commonly supported on metal oxides, but their utility as catalysts is limited by coarsening at high temperatures. Rhodium oxide and rhodium metal nanoparticles on niobate and tantalate supports are anomalously stable. To understand this, the nanoparticle–support interaction was studied by isothermal titration calorimetry (ITC), environmental transmission electron microscopy (ETEM), and synchrotron X-ray absorption and scattering techniques. Nanosheets derived from the layered oxides $KCa_2Nb_3O_{10}$, $K_4Nb_6O_{17}$, and $RbTaO_3$ were compared as supports to nanosheets of Na-TSM, a synthetic fluoromica $(Na_{0.66}Mg_{2.68}(Si_{3.98}Al_{0.02})O_{10.02}F_{1.96})$, and α-$Zr(HPO_4)_2 \cdot H_2O$. High surface area SiO_2 and γ-Al_2O_3 supports were also used for comparison in the ITC experiments. A Born–Haber cycle analysis of ITC data revealed an exothermic interaction between $Rh(OH)_3$ nanoparticles and the layered niobate and tantalate supports, with ΔH values in the range -32 kJ·mol^{-1} Rh to -37 kJ· mol^{-1} Rh. In contrast, the interaction enthalpy was positive with SiO_2 and γ-Al_2O_3 supports. The strong interfacial bonding in the former case led to "reverse" ripening of micrometer-size $Rh(OH)_3$, which dispersed as 0.5 to 2 nm particles on the niobate and tantalate supports. In contrast, particles grown on Na-TSM and α-$Zr(HPO_4)_2 \cdot H_2O$ nanosheets were larger and had a broad size distribution. ETEM, X-ray absorption spectroscopy, and pair distribution function analyses were used to study the growth of supported nanoparticles under oxidizing and reducing conditions, as well as the transformation from $Rh(OH)_3$ to Rh nanoparticles. Interfacial covalent bonding, possibly strengthened by d-electron acid/base interactions, appear to stabilize $Rh(OH)_3$, Rh_2O_3, and Rh nanoparticles on niobate and tantalate supports.

INTRODUCTION

The metal/oxide interface is vital to many current and developing technologies, including nanoscale electronic contacts, biomedical implants and sensors, fuel cell catalysis, photocatalysis, and heterogeneous catalysis.[1−5] Many heterogeneous catalysts consist of late transition metal nanoparticles supported on high surface area oxides, and these particles can coarsen under catalytic reaction conditions. The coarsening presents lifetime and regeneration issues for reactions such as CO oxidation using Cu and Ag catalysts,[6,7] selective oxidation of alcohols on supported Ag catalysts,[8] and water–gas shift and methanol synthesis reactions with supported Cu or Fe nanoparticles.[9] Oxide-supported Rh, Ni, Pd, and Pt catalysts are also prone to coarsening at higher temperatures.[2,3,10]

Much effort has been devoted to inhibiting the growth of metal particles in these catalytic systems. One way nanoparticle catalyst growth can be limited is to disperse the nanoparticles in a porous network, such as a zeolite or high surface area oxide support.[11] In a recent example, gold nanoparticles were stabilized by physically segregating them between sheets of alumina with rough surfaces.[12]

Chemically specific interactions between metal nanoparticles and oxide supports are also well-known to stabilize metal nanoparticle catalysts. The strong metal–support interaction (SMSI) refers to the stabilization of late transition metals (Rh, Au, Pd, and Pt) by certain oxide supports. The SMSI was first described by Tauster and Fung in the late 1970s[13−15] and refers to the physical covering, or encapsulation, of late transition metal particles by a metal oxide.[16−22] This process is thought to be driven by local reduction of the oxide and thus requires a reducible metal oxide such as TiO_2 or Nb_2O_5. Both electron microscopy data and the observation that H_2 and CO chemisorption are suppressed on supported metal nanoparticles are consistent with this encapsulation model. The SMSI has been correlated with differences in surface energies and work functions between the late transition metal and the early transition metal oxide, and this is consistent with the reduction model;[19] however, recent SMSI observations with Au/ZnO do not fit this trend.[23]

Local, covalent bonding at the metal/oxide interface can also stabilize supported metal or metal oxide nanoparticles in the absence of encapsulation by the support. Recently, Campbell has described the electronic metal−support interaction (EMSI), which involves both electronic and geometric interactions between a nanoparticle and support.[24] Electronic structure calculations by Jarvis and Carter have pointed out the importance of covalent bonding through d-electron interactions in stabilizing the adhesion of late transition metals to early transition metal oxides.[25] These d-electron acid−base effects are reminiscent of earlier observations of the anomalous stability of early-late transition metal alloys such as $ZrPt_3$.[26,27] Our group recently discovered anomalous stabilization of rhodium hydroxide/oxide nanoparticles deposited on sheets of the layered oxides $KCa_2Nb_3O_{10}$[4] and $K_4Nb_6O_{17}$.[28] In these studies, 1 to 2 nm nanoparticles remained well dispersed on the nanosheets when heated in air to 350 °C, despite the fact that Rh was not reduced to the metal.

To date, there have been limited experimental data that can directly quantify the strengths of covalent nanoparticle−support interactions. Recently, Campbell and co-workers used microcalorimetry to directly interrogate the bonding between metal atoms and clean, crystallographically well-defined oxide surfaces in ultrahigh vacuum (UHV). Using this technique, they found evidence of strong interfacial bonding between Au nanoparticles and CeO_2.[29,30]

In this paper we report the use of isothermal titration calorimetry (ITC)[31,32] to measure directly the enthalpy of interaction between rhodium hydroxide nanoparticles and metal oxides under wet chemical synthetic conditions. Unilamellar metal oxide nanosheets, prepared by exfoliation of layered oxides and metal phosphates, were used as supports in order to enable imaging of the supported nanoparticles by high-resolution transmission electron microscopy (HRTEM). The compositional variety of these nanosheets allows us to compare the behavior of reducible and nonreducible metal oxides, and the behavior of transition metal oxide supports to that of layered silicates and metal phosphates. HRTEM, X-ray absorption, and X-ray scattering methods were used to study the evolution of particle size and interfacial bonding as a function of temperature under both oxidizing and reducing atmospheres. These studies establish a clear connection between the strength of interfacial bonding and the chemical behavior of supported rhodium hydroxide/oxide nanoparticles.

◼ MATERIALS AND METHODS

Materials Synthesis. Layered metal oxides were synthesized by solid-state reactions as previously described. $K_4Nb_6O_{17}$ was synthesized from K_2CO_3 (99% purity, with a mole fraction excess of 0.1) and Nb_2O_5 (99.9985% purity), at 1100 °C for 24 h.[33,34] $KCa_2Nb_3O_{10}$ was prepared by heating a mixture of K_2CO_3 (with a mole fraction excess of 0.4), $CaCO_3$ (98% purity), and Nb_2O_5 at 1200 °C for 12 h.[35,36] To prepare $RbTaO_3$, Rb_2CO_3 (99.8% purity) and Ta_2O_5 (99% purity) were ground in a molar ratio of 1.02:1 and heated at 900 °C for 20 h (10 °C·min^{-1} ramp).[37] As-obtained samples were then proton-exchanged by mixing 1.0 g of powder with 100 mL of 1.0 mol·L^{-1}· HNO_3 for three days and exchanging the acid solution daily. The powders were then dried at 80 °C. Crystalline α-zirconium phosphate, α-$Zr(HPO_4)_2$·H_2O (α-ZrP), was available from a previous study.[38] Na-TSM, with the formula $Na_{0.66}Mg_{2.68}(Si_{3.98}Al_{0.02})O_{10.02}F_{1.96}$ and a cation exchange capacity of 1.20 mmol of cation·g^{-1}, was used. Tetra(n-butylammonium) hydroxide (TBA^+OH^-) was obtained as a mole fraction of 0.4 in water

Deposition of Rhodium Hydroxide Nanoparticles. The proton-exchanged materials (0.100 g) were stirred in 25 mmol·L^{-1}

TBA^+OH^- solution (50 mL) overnight or longer to complete the exfoliation reaction. The pH of the solution after exfoliation was 12.0. The suspension was allowed to settle overnight before decanting the exfoliated sheets away from any unexfoliated starting material. Commercialy purchased γ-Al_2O_3 (0.10 g, 99.5% purity) and SiO_2 (0.10 g, 99.5% purity) were stirred in 25 mmol·L^{-1} TBA^+OH^- solution (50 mL) for at least 1 h prior to rhodium hydroxide deposition. Na-TSM (0.1 g) was exfoliated by adding to 10 mL of water, and then the solution pH was brought to 12.0 with concentrated NaOH.

Rhodium hydroxide deposition was performed as previously reported.[4,28] Aqueous $RhCl_3$ solution (20 mmol·L^{-1}) was added to achieve the desired rhodium mass deposition. All mass fractions correspond to the mass fraction of Rh deposited. The suspension was stirred for 18 h during which it turned yellow due to hydrolysis of $RhCl_3$ to form $Rh(OH)_3$.[4] This suspension was then added dropwise to 2.0 mol·L^{-1} KOH (50 mL) to restack and flocculate the nanosheets. The solid sample was separated from the suspension by centrifugation and then washed twice more with KOH solution and three times with water to remove excess KOH. For restacking and flocculation of the acid-exchanged $RbTaO_3$ sample, 0.05 mol·L^{-1} HNO_3 was added dropwise to the solution. The sample was then washed three times with water and dried in air at 60 °C. Exfoliated sheets of Na-TSM that were reacted with $Rh(OH)_3$ did not retain any nanoparticles when restacked with KOH, so the sample was simply centrifuged to recover all the solids for analysis. All samples were heated in air at progressively higher temperatures (see below) to convert rhodium hydroxide to rhodium oxide and were also heated in H_2 atmospheres to study reduction of the oxide.

Characterization. X-ray powder diffraction (XRD) patterns were obtained with a theta−theta diffractometer (monochromatized Cu Kα radiation, λ = 0.15418 nm). For inductively coupled plasma emission spectroscopy (ICP-AES) analysis, samples were dissolved by a lithium metaborate fusion technique and analyzed for rhodium. Zeta potential measurements were conducted using a microelectrophophoresis instrument and a laser light source operating at a wavelength of 633 nm. Surface area was determined from Brunauer−Emmett−Teller (BET) adsorption isotherms. Ambient temperature transmission electron microscopy (TEM) images were obtained using an electron microscope with a LaB_6 electron source and an accelerating voltage of 200 kV. Samples were prepared by dropping an aqueous solution onto a lacey-carbon-coated copper grid and drying at room temperature overnight before use.

In situ HRTEM images were obtained on an environmental transmission electron microscope (ETEM) with spherical aberration (Cs) correction and an information limit of 0.12 nm at an accelerating voltage of 200 kV. For vacuum annealing, a membrane-based single tilt heating holder was used and samples were dispersed by drop-casting from solution onto a temperature-controlled sample support and dried under a heat lamp. For annealing in hydrogen atmosphere, a double tilt furnace heating holder was used and samples were drop-cast from solution onto a 30 nm thick Si nanoporous grid with 10 nm holes or molybdenum grids before being dried under a heat lamp. Pure hydrogen at 200 Pa was used during the in situ hydrogen annealing experiments.

Nanoparticle structure identification was done using fast Fourier transforms (FFT) of areas of interest from high resolution ETEM images. Crystal Ball, developed at CNST-NIST, was used to identify the crystallographic phases. Errors of 1% for lattice spacings and 5% for angles were used when matching reference phases to the experimental values obtained from FFTs. Diffraction patterns were simulated to confirm a match with the experimental FFT.

Temperature-programmed reaction spectroscopy (TPRS) experiments were conducted in a plug-flow reactor connected to a mass spectrometer. Light-off curves for oxidation of adsorbed CO to CO_2 were measured on Rh_2O_3/$KCa_2Nb_3O_{10}$ samples that were first heated in hydrogen (volume fraction of 0.05, balance argon, 99.999%) at 600 °C for 2 h. The samples were purged with He (99.999%, UHP) while being cooled to ambient temperature. During the experiment, the sample was sandwiched between two plugs of quartz wool. Gas flow
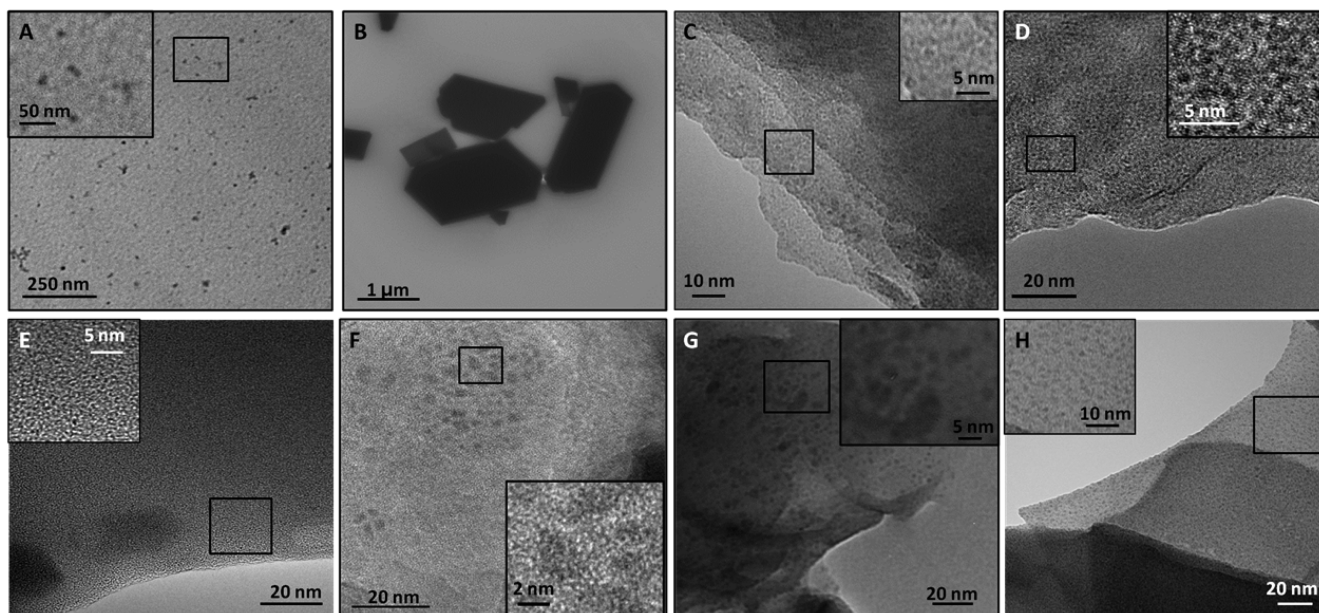
Figure 1. TEM images of $RhCl_3·3H_2O$ in 25 $mmol·L^{-1}$ TBA^+OH^- after (A) 1 min and (B) 10 min. Panel C shows the "reverse" ripening of larger $Rh(OH)_3$ particles deposited onto $TBA_{0.24}H_{0.76}Ca_2Nb_3O_{10}$ to give highly dispersed nanoparticles. TEM images of $Rh(OH)_3$ deposited on $KCa_2Nb_3O_{10}$ (D), $K_4Nb_6O_{17}$ (E), Na-TSM (F), α-ZrP (G), and $HTaO_3$ (H) at ambient temperature.

rates of CO (~7 kPa)/O_2 (40 kPa) and remaining He were controlled by mass flow controllers using a homemade program. After the sample reached room temperature, the lean CO/O_2/He flow (~50 cm^3· min^{-1}) was started. Heating was initiated with a linear temperature ramp of 10 °C·min^{-1} to a final temperature of 400 °C. The effluent was sampled by mass spectrometry, and ion counts for CO, O_2, and CO_2 were measured. No steps were taken to determine whether the light-off curves were influenced by mass transport effects.

X-ray absorption spectroscopy (XAS) experiments were performed at the Advanced Photon Source, Argonne National Lab, on the bending magnet station, sector 10-BM. Measurements were taken at the Rh–K edge: 23 230 eV. Samples were heated to a specific temperature in hydrogen (volume fraction of 0.035, balance nitrogen) at 100 kPa for 30 min and then cooled to room temperature prior to XAS measurements. Rh foil and Rh_2O_3 were used as standards for Rh–Rh and Rh–O interatomic distances and coordination numbers in the analysis. For extended X-ray absorption fine structure (EXAFS) analysis, backscattering amplitude and phase shift references were produced from the standards. All EXAFS fitting was performed by first fixing the Debye–Waller factor (DWF) to 0.001. The k^2-weighted data in R-space were fitted by least-squares optimization to obtain values for coordination numbers (CN) and interatomic distances. The DWF was then allowed to vary in order to perform the final fit. The EXAFS data were fitted from a k-space of 0.27 nm to a minimum of 1.2 nm, with as much data being incorporated in the 1.2 to 1.5 nm range as possible. The data sets were normalized using the pre-edge energy, and k-ranges were determined from the Rh foil to allow for direct comparison of the data at different temperatures.

Pair distribution function (PDF) experiments were performed at the Advanced Photon Source, Argonne National Laboratory, on beamline 11-ID-B. Samples were placed in 1.1 mm outer diameter (o.d.), 0.9 mm inner diameter (i.d.) quartz capillary tubes packed with calcined quartz wool. High-energy X-ray scattering data (λ = 0.02127 nm, E = 58 keV) were taken with samples heated under hydrogen (volume fraction of 0.035) at a rate of 3 °C·min^{-1}. Diffraction patterns from supported Rh/Rh oxide particles and unmodified supports were recorded and analyzed, and the resulting PDF from the support was then subtracted from the PDF obtained from the supported nanoparticle composite to determine the contributions from the Rh/ Rh oxide with limited interference from the supports.[39]

Isothermal titration calorimetry (ITC) experiments were performed in triplicate using an ITC instrument with a 1.04 mL hastelloy cell.

Typically, metal oxide support suspensions were loaded in the cell between 0.1 $mmol·L^{-1}$ and 10 $mmol·L^{-1}$ with a 15 $mmol·L^{-1}$ to 16 $mmol·L^{-1}$ aqueous $RhCl_3$ solution in the syringe. All experiments were performed at 25 °C using either a 100 or 250 μL syringe with 25 min between injections. Data were fitted with either an independent or multiple-site bonding model. Heats of dilution were subtracted from all experiments to obtain thermochemical data.
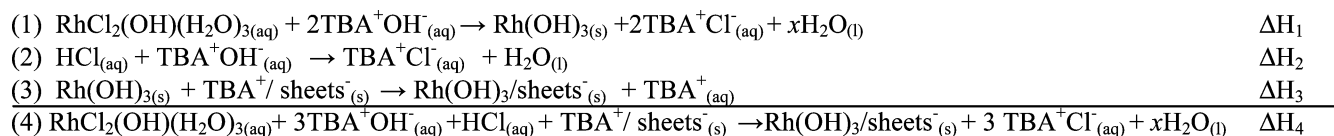
The uncertainty for each of the measured values is given as one standard deviation of the mean. The number of measurements, n, is reported throughout the text.

RESULTS AND DISCUSSION

Nanoparticle/Support Compositions. The phase purity of $KCa_2Nb_3O_{10}$,[35] $K_4Nb_6O_{17}$,[33,34] $RbTaO_3$,[37] and α-ZrP[38] was confirmed by comparing powder XRD patterns with literature reports. The layered oxides $KCa_2Nb_3O_{10}$, $K_4Nb_6O_{17}$, and $RbTaO_3$ were acid-exchanged to yield $HCa_2Nb_3O_{10}·0.5H_2O$,[40] $K_{1.1}H_{2.9}Nb_6O_{17}·nH_2O$,[28] and $Rb_{0.1}H_{0.9}TaO_3·1.3H_2O$,[37] and the phase purity was again established by XRD (Supporting Information, Figure S1). These samples were then exfoliated to give nanosheets of $TBA_{0.24}H_{0.76}Ca_2Nb_3O_{10}$, $TBA_{0.7}H_{2.2}K_{1.1}Nb_6O_{17}$, and $TBA_{0.1}H_{0.8}Rb_{0.1}TaO_3$ in excess TBA^+OH^- solution. The stoichiometry of the exfoliated samples was obtained by titrating the residual basic solution after nanosheet exfoliation. From this back-titration, the amount of free base, and hence the amount of TBA^+ removed from solution by association with the nanosheets, was determined. The exfoliation of α-ZrP has been described in detail previously.[38] Na-TSM was exfoliated by addition to water to produce micrometer-sized sheets.[41]

$Rh(OH)_3$ nanoparticles were deposited on oxide supports by adding an aqueous solution of $RhCl_3·3H_2O$ to a suspension of nanosheets in excess TBA^+OH^-. The mass fraction of $Rh(OH)_3$ deposited is always 0.05 unless otherwise stated. Previous studies have established that this procedure gives <1 nm diameter rhodium hydroxide nanoparticles on both $KCa_2Nb_3O_{10}$ and $K_4Nb_6O_{17}$ supports.[4,28] As previously reported, XRD patterns of these materials show only 00l and

Scheme 1. Born−Haber Cycle for Deposition of Rhodium Hydroxide Particles onto Nanosheet Supports in ITC Experiments

(1) $RhCl_2(OH)(H_2O)_{3(aq)} + 2TBA^+OH^-_{(aq)} \rightarrow Rh(OH)_{3(s)} + 2TBA^+Cl^-_{(aq)} + xH_2O_{(l)}$ $\qquad \Delta H_1$

(2) $HCl_{(aq)} + TBA^+OH^-_{(aq)} \rightarrow TBA^+Cl^-_{(aq)} + H_2O_{(l)}$ $\qquad \Delta H_2$

(3) $Rh(OH)_{3(s)} + TBA^+/sheets^-_{(s)} \rightarrow Rh(OH)_3/sheets^-_{(s)} + TBA^+_{(aq)}$ $\qquad \Delta H_3$

(4) $RhCl_2(OH)(H_2O)_{3(aq)} + 3TBA^+OH^-_{(aq)} + HCl_{(aq)} + TBA^+/sheets^-_{(s)} \rightarrow Rh(OH)_3/sheets^-_{(s)} + 3 TBA^+Cl^-_{(aq)} + xH_2O_{(l)}$ $\quad \Delta H_4$

$hk0$ reflections after turbostratic restacking of the layered oxide and an increase in d-spacing as the loading of $Rh(OH)_3$ increases (Supporting Information, Figure S2).

As a control experiment, aqueous $RhCl_3 \cdot 3H_2O$ solution was added to excess TBA^+OH^- and the time course of hydrolysis and particle growth was measured by TEM. As seen in Figure 1A,B, the lateral dimensions of $Rh(OH)_3$ particles were (11 ± 3) nm after 1 min and grew to >1 μm after 10 min. These results suggest that when the hydrolysis occurs in the $TBA_{0.24}H_{0.76}Ca_2Nb_3O_{10}$ and $TBA_{0.7}H_{2.2}K_{1.1}Nb_6O_{17}$ suspensions, the initially formed approximately 1 μm $Rh(OH)_3$ particles undergo "reverse" ripening to become well dispersed, <1 nm nanoparticles. This hypothesis was verified by starting with independently synthesized micrometer-size $Rh(OH)_3$ particles, which were added to a basic solution of $TBA_{0.24}H_{0.76}Ca_2Nb_3O_{10}$ to yield well-dispersed oxide-supported nanoparticles (Figure 1C). The breakup or dissolution of the larger $Rh(OH)_3$ particles appears to be driven thermodynamically by a favorable interaction between the nanoparticles and the support, which compensates for the increased surface energy of the nanoparticles.

Complete deposition of rhodium hydroxide onto $TBA_{0.24}H_{0.76}Ca_2Nb_3O_{10}$ and $TBA_{0.7}H_{2.2}K_{1.1}Nb_6O_{17}$ was confirmed by both the formation of a clear solution, as $Rh(OH)_3$ is yellow in solution, and ICP-AES, which confirmed that a mass fraction of 0.05 rhodium hydroxide was deposited onto the sample. In contrast, incomplete deposition of $Rh(OH)_3$ on the layered silicate Na-TSM was evidenced by the yellow color of the supernatant solution after centrifugation of the layered silicate, as well by the presence of high contrast, micrometer-size crystals with hexagonal texture (resembling those shown in Figure 1B) in the TEM analysis of the Na-TSM precipitate.

Zeta-potential measurements show that the nanosheet suspensions of the oxide supports $KCa_2Nb_3O_{10}$ and $K_4Nb_6O_{17}$, as well as the $Rh(OH)_3$ particles, are negatively charged at the pH of the reaction.[4] Thus, a simple electrostatic interaction between the nanoparticles and niobate sheets cannot explain the small size and even distribution of nanoparticles on $KCa_2Nb_3O_{10}$ and $K_4Nb_6O_{17}$ supports (Figure 1D,E). In contrast, an uneven distribution of rhodium hydroxide nanoparticles was found on the Na-TSM and α-ZrP supports, with many areas not having any particles (Figure 1F,G). In both cases, a colored solution remained after rhodium hydroxide deposition and centrifugation, meaning that not all the rhodium hydroxide deposited onto the support. Because the SMSI mechanism is thought to involve local reduction of metal ions in the supporting oxide,[14,17−19,30,42−44] an additional experiment was performed with $TBA_{0.1}H_{0.8}Rb_{0.1}TaO_3$ nanosheets in place of layered niobates. Despite the fact that Ta(V) is much more difficult to reduce than Nb(V), the resulting materials, prepared under aerobic conditions, showed a uniform distribution of nanoscale particles (1.3 ± 0.3) nm, $n = 101$, Figure 1H). The tantalate nanosheets are also negatively charged at the pH of the reaction (pH = 12.0). These data are consistent with the idea that the stabilization of $Rh(OH)_3$ nanoparticles arises from a specific chemical interaction with

the support that is not driven by electrostatic interactions or local reduction.

Isothermal Titration Calorimetry. Isothermal titration calorimetry (ITC) was used to investigate the strength of bonding between rhodium hydroxide nanoparticles and oxide supports.

During a deposition reaction, several reactions occur simultaneously, and the overall process can be represented by the Born−Haber cycle shown in Scheme 1. The enthalpy associated with the interaction of the $Rh(OH)_3$ nanoparticles and the oxide support (reaction 3) is determined by taking the difference between the overall reaction (reaction 4) and the heats of hydrolysis (reaction 1, $\Delta H_1 = (-27 \pm 5)$ kJ·mol^{-1}) and neutralization (reaction 2, $\Delta H_2 = (-58 \pm 2)$ kJ·mol^{-1}) (see Supporting Information for details of the determination of ΔH_1 and ΔH_2). In this cycle, there is also a surface energy term that is dependent on the size of the particles produced. In order to obtain a reliable comparison of bonding energies for different supports, the final sizes of the $Rh(OH)_3$ nanoparticles should be similar. $Rh(OH)_3$ particles deposited on Na-TSM $((5 \pm 1)$ nm, $n = 101$) are significantly larger than those deposited on Nb oxide nanosheets (<1 nm diameter).

Therefore, high surface area SiO_2 and γ-Al_2O_3 were used as nontransition metal oxide supports in the ITC experiments, as they gave $Rh(OH)_3$ nanoparticle sizes of (0.7 ± 0.2) nm ($n = 100$) and (1.3 ± 0.4) nm ($n = 100$), respectively. (Supporting Information, Figure S3). The γ-Al_2O_3 used in these experiments had an average particle diameter of (50 ± 40) nm ($n = 127$) and a surface area of (35.8 ± 0.1) m^2·g^{-1}. The SiO_2 support had an average particle diameter of (17 ± 6) nm ($n = 101$) and a surface area of (408 ± 8) m^2·g^{-1}. Both of these high surface area oxides are used widely as supports for rhodium and platinum nanoparticles. In addition, nanoparticles deposited on these supports are known to coalesce at temperatures as low as 550 °C.[2,45−47]

A representative ITC isotherm for $Rh(OH)_3$ deposition onto $TBA_{0.24}H_{0.76}Ca_2Nb_3O_{10}$ sheets and the associated integrated area plot are shown in Figure 2, and the heats of $Rh(OH)_3$ adsorbing to various oxide supports are listed in Table 1. The adsorption of $Rh(OH)_3$ to $TBA_{0.24}H_{0.76}Ca_2Nb_3O_{10}$, $TBA_{0.7}H_{2.2}K_{1.1}Nb_6O_{17}$, and $TBA_{0.1}H_{0.8}Rb_{0.1}TaO_3$ is exothermic, with ΔH_3 values in the range of -32 kJ·mol^{-1} Rh to -37 kJ·mol^{-1} Rh. These three layered oxides are structurally different: $KCa_2Nb_3O_{10}$ contains only corner-sharing NbO_6 octahedra, whereas the corrugated sheets of $K_4Nb_6O_{17}$ and $RbTaO_3$ contain both edge and corner-shared octahedra. Nevertheless, the ΔH_3 values are all exothermic and quite similar. In contrast, ΔH_3 values obtained with SiO_2 and γ-Al_2O_3 were both endothermic, (25 ± 6) kJ·mol^{-1} and (55 ± 6) kJ·mol^{-1}, respectively. These differences are consistent with a relatively strong covalent interaction between $Rh(OH)_3$ and the layered niobate and tantalate supports. The difference in ΔH_3 between SiO_2 and γ-Al_2O_3 may, in part, reflect a difference in the electrostatic energy of bringing negatively charged $Rh(OH)_3$ particles to the surfaces of these supports. SiO_2 and γ-Al_2O_3 have zeta-potentials of (-37 ± 1) mV and (-44 ± 1) mV,
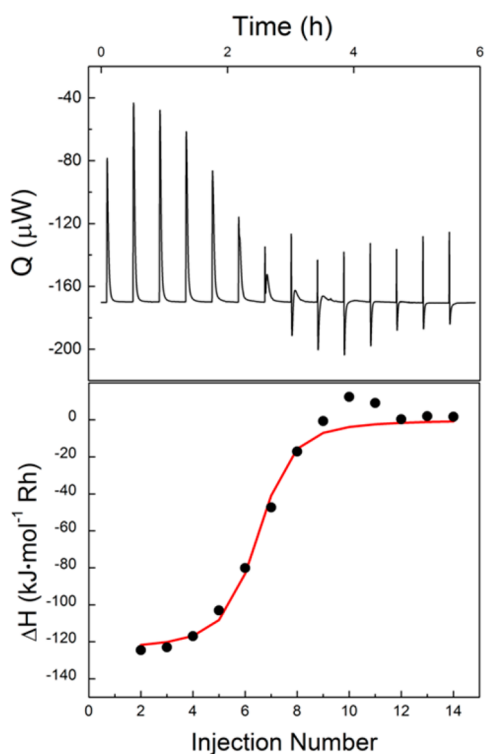
Figure 2. (A) Real-time ITC thermogram for the addition of $RhCl_3$ aqueous solution to $TBA_{0.24}H_{0.76}Ca_2Nb_3O_{10}$ sheets in excess TBA^+OH^- solution and (B) the integrated heat data with an independent model fit.

Table 1. Thermochemical Data from ITC Experiments for $Rh(OH)_3$ Deposition onto Metal Oxide Supports $(\Delta H_3)^a$

oxide support	ΔH_3 $(kJ \cdot mol^{-1})$
$TBA_{0.24}H_{0.76}Ca_2Nb_3O_{10}$	-35 ± 9
$TBA_{0.7}H_{2.2}K_{1.1}Nb_6O_{17}$	-37 ± 9
$TBA_{0.1}H_{0.8}Rb_{0.1}TaO_3$	-32 ± 10
γ-Al_2O_3	55 ± 6
SiO_2	25 ± 6

^{a}The errors are reported as one standard deviation of the mean for triplicate measurements.

respectively. The less negative zeta-potential of SiO_2 results in less electrostatic repulsion and therefore a smaller endothermic heat of interaction than with γ-Al_2O_3.

In Situ TEM in Vacuum. In situ TEM was performed to monitor the size evolution of $Rh(OH)_3$ nanoparticles as a function of temperature in vacuum. By statistically analyzing the particle size, the growth of nanoparticles was correlated with data from other physical characterization methods (see below) to identify the chemical changes that occurred upon heating. Three different supports were used in these experiments: two layered niobates ($KCa_2Nb_3O_{10}$ and $K_4Nb_6O_{17}$) and one (Na-TSM) that was chemically similar to the high surface area silica and alumina supports that did not show evidence of strong covalent bonding to $Rh(OH)_3$ in the ITC experiments.

Figure 3A shows a plot of average $Rh(OH)_3/Rh_2O_3$ nanoparticle diameter versus temperature for samples that were heated in vacuum in the TEM. Average particle sizes are not shown for temperatures below 200 °C for the niobate supports because the nanoparticles were too small to obtain reliable size information. At 200 °C, both the $KCa_2Nb_3O_{10}$ and

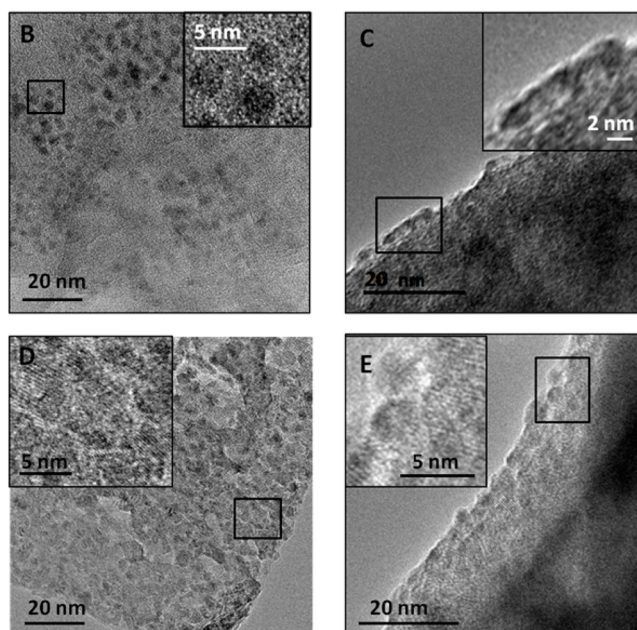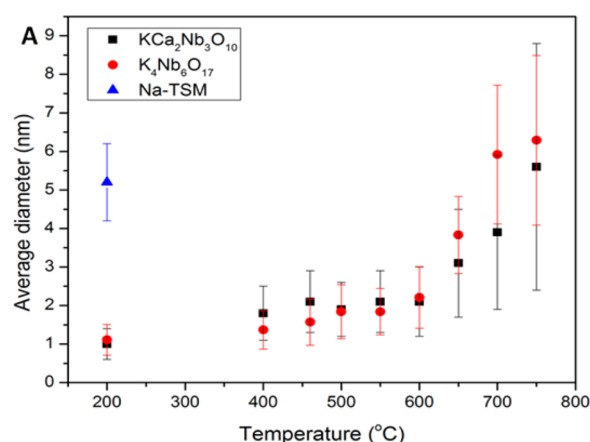**Figure 3.** (A) Plot of the average diameter of rhodium hydroxide/ oxide nanoparticles with increasing temperature on $KCa_2Nb_3O_{10}$, $K_4Nb_6O_{17}$, and Na-TSM supports. The uncertainty reported for each measured value is one standard deviation of the mean for n measurements. See Supporting Information, Table S1, for the number of measurements for each value. TEM images showing (B) the uneven distribution of nanoparticles at 200 °C on Na-TSM, (C) rhodium oxide nanoparticles on $K_4Nb_6O_{17}$ at 500 °C that begin to neck together, and the distribution of Rh_2O_3 particles on (D) $KCa_2Nb_3O_{10}$ and (E) $K_4Nb_6O_{17}$ at 600 °C.

$K_4Nb_6O_{17}$ supports have evenly distributed nanoparticles with average diameters of (1.0 ± 0.4) nm and (1.1 ± 0.4) nm, respectively. The average diameter of nanoparticles deposited on Na-TSM at 200 °C is (5 ± 1) nm, and the particles are unevenly distributed on the support; i.e., there are some areas that have no nanoparticles present (Figure 3B). At temperatures above 200 °C, it is difficult to obtain statistical size information for nanoparticles deposited on Na-TSM because of the uneven distribution of larger particles. A TEM image of Rh_2O_3 nanoparticles on Na-TSM at 440 °C shows these larger particles (see Supporting Information, Figure S4).

As the temperature increases, nanoparticles on the niobate supports become visible in the TEM images but are still less than 2 nm in diameter. At 400 °C, crystallization and faceting of the nanoparticles was noticeable. This is tentatively attributed

to the phase change from $Rh(OH)_3$ to Rh_2O_3, but no lattice spacing corresponding to crystals of the latter could be found at this temperature.

Although the average diameters of the nanoparticles remained similar up to 600 °C, necking of the nanoparticles deposited on $K_4Nb_6O_{17}$ began at 500 °C, as shown in Figure 3C. This necking allows for diffusion of rhodium atoms between particles. At 500 °C, a change in the crystalline support is seen in both XRD and TEM. While the support is changing, the nanoparticle size remains constant, which again supports the idea that the nanoparticles are covalently anchored to the niobate sheets.

Figure 3D,E shows the dispersion of approximately 2 nm diameter nanoparticles on $KCa_2Nb_3O_{10}$ and $K_4Nb_6O_{17}$ at 600 °C. At 650 °C, the average diameter of nanoparticles on both $KCa_2Nb_3O_{10}$ and $K_4Nb_6O_{17}$ begins to increase. The three nanoparticles that were necking together at 500 °C (Figure 3C) have coalesced into one larger particle at 650 °C. By 725 °C, hexagonal particles become obvious, which is indicative of corundum-structure Rh_2O_3 at this temperature. The particles were confirmed to be crystalline Rh_2O_3 at 750 °C (Supporting Information, Figure S5).[48]

TEM statistical analysis shows that Rh_2O_3 nanoparticles grow at the same rate on $KCa_2Nb_3O_{10}$ and $K_4Nb_6O_{17}$. In contrast, the original distribution and growth of nanoparticles is drastically different on Na-TSM.

In Situ TEM in Reducing Atmosphere. Rh metal nanoparticles on oxide supports are used widely in catalysis, and the temperature at which they can be used under reducing conditions is limited by their stability against growth. Therefore, in situ TEM was used to investigate the growth of Rh nanoparticles on both Nb oxide nanosheets and Na-TSM under reducing conditions.

Figure 4A shows a plot of average nanoparticle diameter versus temperature for samples heated in hydrogen. The nanoparticles were too small to retrieve size information when deposited on $KCa_2Nb_3O_{10}$ and imaged at temperatures up to 200 °C. The nanoparticles deposited on $K_4Nb_6O_{17}$ were (0.5 ± 0.2) nm in diameter at 200 °C when heated in 200 Pa of hydrogen, compared to (1.1 ± 0.4) nm when heated in vacuum $(1 \times 10^{-6}$ Pa$)$. When samples were heated in H_2, the growth of the nanoparticles was retarded for all supports relative to samples heated in vacuum (Figures 4B−E). Interestingly, nanoparticles deposited on $KCa_2Nb_3O_{10}$ and $K_4Nb_6O_{17}$ remain smaller than 2 nm diameter up to 700 °C. Because the nanoparticles do not aggregate, they retain active surface area at increased temperatures, and thus niobates are likely to stabilize Rh nanoparticles under catalytic conditions.

Nanoparticles deposited on Na-TSM also remain small $((3.6 \pm 0.9)$ nm$)$ at 600 °C, but they are not evenly dispersed. Below 600 °C, the particles are present only at the sheet edges (Figure 4D). At 600 °C, the nanoparticles move from the edges onto basal planes of the sheets (Figure 4E). This behavior differs from the other supports heated in H_2, where the nanoparticles were less than 2 nm and evenly distributed at all temperatures studied. $Rh(OH)_3$ nanoparticles deposited on Na-TSM and heated under vacuum also behaved differently. Under vacuum, the nanoparticles were unevenly distributed but did not segregate to the edges of the sheets. The Rh_2O_3 nanoparticles also grew rapidly with temperature under vacuum conditions.

Possible beam effects were investigated to confirm that the increase in particle size was due to the intended increase in temperature and not due to irradiation. An area of the support
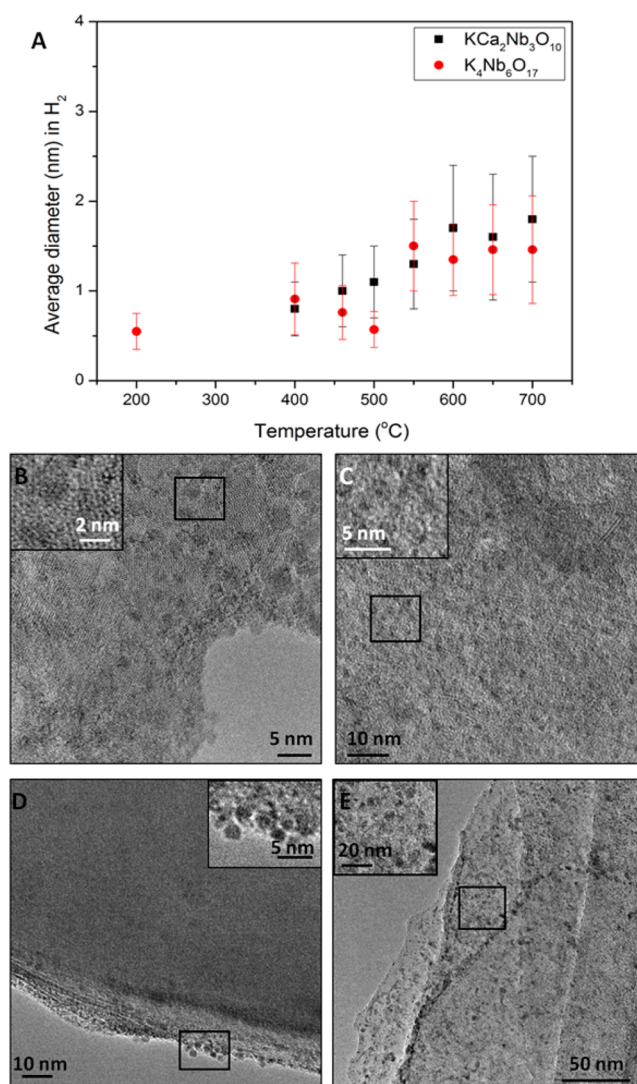

Figure 4. (A) Plot of the average diameter of nanoparticles heated in situ in 200 Pa H_2 at increasing temperatures on $KCa_2Nb_3O_{10}$ and $K_4Nb_6O_{17}$. The uncertainty reported for each measured value is one standard deviation of the mean for n measurements. See Supporting Information, Table S2 for number of measurements for each value. TEM images of nanoparticles on (B) $KCa_2Nb_3O_{10}$ at 600 °C, (C) $K_4Nb_6O_{17}$ at 600 °C, (D) Na-TSM at 200 °C, and (E) Na-TSM at 600 °C.

$K_4Nb_6O_{17}$ with deposited nanoparticles was bombarded with the electron beam for 12 min at 550 °C (electron density of 3×10^7 electrons·nm^{-1}), which is the approximate length of time spent at each temperature during TEM imaging. During this time, no nanoparticle growth was evident. This leads to the conclusion that beam effects did not induce significant changes in nanoparticle size.

Short time scale studies were also performed in situ in the TEM to determine if kinetics played a role in the growth of the nanoparticles. During a typical TEM analysis, stabilization at a given temperature took up to 30 min. Samples with nanoparticles deposited on $KCa_2Nb_3O_{10}$ and Na-TSM were heated at 600 °C for 2.5 h, and the particle sizes did not increase on either support. To further investigate kinetic effects, nanoparticles deposited on $KCa_2Nb_3O_{10}$ were heated ex situ at atmospheric pressure in pure hydrogen at 600 °C for 24 and 48 h, and the average diameters of the nanoparticles were (4 ± 2)

nm (n = 116) and (4 ± 3) nm (n = 192), respectively. This treatment should produce nanoparticles that consist primarily of elemental Rh; XAS measurements (see below) of supported particles, reduced under less rigorous conditions, show a 90% conversion of Rh_2O_3 to Rh by 500 °C. Following reduction in hydrogen, TPRS experiments were used to confirm that Rh supported on $KCa_2Nb_3O_{10}$ falls within the expected range of light-off temperatures for CO oxidation over supported Rh and Rh oxides.[49] These data (see Supporting Information) confirm that the Rh/Rh_2O_3 nanoparticles are accessible and capable of catalyzing the oxidation of adsorbed CO when supported on $KCa_2Nb_3O_{10}$.

Rhodium oxide nanoparticles have previously been deposited on SiO_2, $CeZrO_2$, ZrO_2, and CeO_2 supports and heated in H_2 to reduce the particles. The activity of these supported Rh catalysts for CO oxidation was found to increase in the order SiO_2 < ZrO_2 < $CeZrO_2$ < CeO_2. It was suggested that the activity increases in this manner because of the distribution of rhodium oxide on the support. This trend correlates with the d-electron acidity of the support, which increases in the order of increasing catalyst activity.[43] Another study showed that zirconia retarded the growth of Pd nanoparticles, whereas SiO_2 and γ-Al_2O_3 supports did not have the same effect at 900 °C.[2,50] These trends are not easily explained by an SMSI model involving reduction of the support. Zirconia is not easily reduced nor does it suppress H_2 chemisorption, but it does maintain small particle sizes for late transition elements such as Rh and Pd.[2]

X-ray Absorption Spectroscopy. The transformation of supported $Rh(OH)_3$ to elemental Rh was studied using extended X-ray absorption spectroscopy (EXAFS). Samples were heated ex situ in hydrogen for 30 min at each temperature before X-ray absorption data were obtained under ambient conditions. Figure 5A,B shows the Fourier transform magnitude of the Rh−K edge EXAFS spectra for samples of $Rh(OH)_3$ deposited on $KCa_2Nb_3O_{10}$ and Na-TSM. The peak at 0.157 nm is due to Rh−O scattering, while the peak at 0.24 nm is due to Rh−Rh scattering.

Figure 5A shows the Rh−Rh peak at 0.24 nm increasing slowly from 250 °C to 500 °C when the particles are deposited on $KCa_2Nb_3O_{10}$. This can be interpreted as a slow increase in rhodium particle size. At 500 °C, the magnitude of the peak at 0.24 nm is only 55% of that of the rhodium foil. In contrast, for the Na-TSM support (Figure 5B), the peak magnitude at 0.24 nm is 80% that of the rhodium foil. EXAFS spectra for $Rh(OH)_3$ and Rh_2O_3 were almost indistinguishable, and therefore Rh_2O_3 was used in the analysis although $Rh(OH)_3$ is present at room temperature. This could be the reason for the slight shift of the Rh−O peak, from 0.150 nm measured with the Rh_2O_3 standard, to 0.154 nm in the room temperature samples of $Rh(OH)_3$ on both supports.

A plot of Rh−Rh coordination number versus temperature is shown in Figure 5C. Bulk rhodium metal has a coordination number of 12. The average Rh−Rh coordination numbers of the nanoparticles deposited on $KCa_2Nb_3O_{10}$ and Na-TSM at 500 °C are 6 and 8, respectively. Coordination numbers smaller than 12 have previously been observed for fine Rh metal particles dispersed on supports.[51] Using the assumption that the Rh particles are cuboctahedra, a coordination number of 9 correlates to approximately 3 nm diameter Rh metal particles.[51] This is in good agreement with the current study in which coordination numbers of 6 and 8 correlate with particle diameters of (1.1 ± 0.4) nm and (2.9 ± 0.8) nm, respectively,
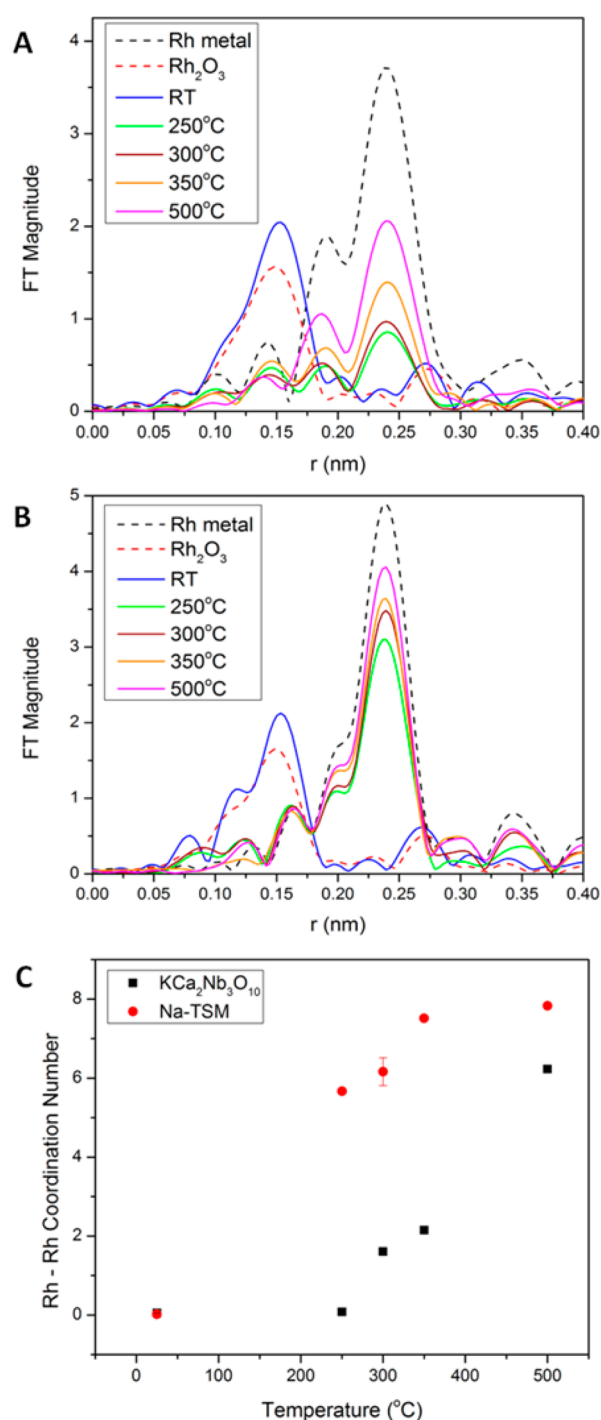

Figure 5. EXAFS spectra of rhodium catalyst on (A) $KCa_2Nb_3O_{10}$ and (B) Na-TSM heated ex situ in hydrogen for 0.5 h at each temperature. The spectra were taken at ambient conditions. (C) Plot of Rh−Rh coordination number versus temperature for $KCa_2Nb_3O_{10}$ and Na-TSM shows the quicker reduction to rhodium metal nanoparticles on Na-TSM versus $KCa_2Nb_3O_{10}$. The errors are reported as one standard deviation of the mean for triplicate measurements.

as measured by TEM. However, it is important to note that the coordination number of Rh in bulk Rh_2O_3 is 6 and can be smaller in Rh_2O_3 nanoparticles. Thus, it is also possible that stabilization of Rh_2O_3 relative to Rh contributes to the lower coordination numbers observed on niobate supports.

X-ray absorption near edge structure (XANES) analysis of samples reduced in 100 kPa H_2 indicates that Rh(III) is 80%

reduced to Rh(0) by 250 °C and 90% by 500 °C on both KCa$_2$Nb$_3$O$_{10}$ and Na-TSM (Supporting Information, Table S3). While the rhodium is being reduced at the same rate for both supports, the coordination number increases more rapidly for the particles on Na-TSM than KCa$_2$Nb$_3$O$_{10}$. As noted above, the difference can be attributed to differences in the size of the precursor Rh(OH)$_3$ particles.

Pair-Distribution Function. High energy X-ray diffraction was performed and analyzed via pair-distribution functions (PDF) to track the rate of reduction of rhodium−oxygen bonds and growth of Rh metal nanoparticles deposited on the oxide supports in a reducing atmosphere. PDF data followed the same qualitative trends as data obtained from TEM and XAS. Rh(OH)$_3$ on KCa$_2$Nb$_3$O$_{10}$, K$_4$Nb$_6$O$_{17}$, and Na-TSM supports were heated in situ in 100 kPa hydrogen for the duration of the experiment. Figure 6A shows plots of normalized G(r) intensity versus temperature for rhodium−rhodium distances of 0.269 nm and rhodium−oxygen distances of 0.182 and 0.224 nm. The rhodium−rhodium distance correlates to the first shell bond length in rhodium metal and the rhodium−oxygen distances correlate to bond lengths in Rh$_2$O$_3$. These plots show the simultaneous decrease of Rh−O and increase of Rh−Rh bonding. Figure 6A shows a sharp decrease in normalized G(r) intensity at the Rh−O bond length and a sharp increase of Rh−Rh bonding for nanoparticles deposited on Na-TSM. Both of these curves begin to plateau around 250 °C. This is in agreement with XANES data that show >80% conversion from rhodium oxide to Rh at 250 °C for particles deposited on Na-TSM. On the other hand, with KCa$_2$Nb$_3$O$_{10}$ and K$_4$Nb$_6$O$_{17}$ nanosheets as supports, the decrease of Rh−O and increase of Rh−Rh normalized G(r) intensity is more gradual (Figure 6B,C). This suggests that the niobate supports stabilize Rh$_2$O$_3$ relative to Rh nanoparticles and thus postpones the reduction of Rh(III) to higher temperatures.

The diameters of Rh nanoparticles were determined by TEM statistical size analysis and correlate with the PDF analysis. TEM analysis shows that at 400 °C, the average size of nanoparticles deposited on KCa$_2$Nb$_3$O$_{10}$ and heated in hydrogen is 0.8 nm. In Figure 6B, the normalized G(r) intensity at 0.8 nm Rh−Rh distance has an inflection point at 400 °C, indicating an increase in nanoparticle diameter to 0.8 nm at this temperature. PDF analysis for nanoparticles deposited on K$_4$Nb$_6$O$_{17}$ also correlates to the TEM analysis. An Rh−Rh interatomic distance of 0.574 nm was investigated for this sample, as shown in Figure 5C. A sharp increase in the normalized G(r) intensity for this Rh−Rh distance occurs at 250 °C. TEM analysis shows the nanoparticle size is 0.55 nm at 200 °C and 0.9 nm at 400 °C. Therefore, the PDF estimate of particle diameter correlates well with the TEM statistical analysis.

■ CONCLUSIONS

Comparison of ITC, TEM, XAS, EXAFS, and PDF data reveal that Rh$_2$O$_3$ and Rh nanoparticles are small and evenly dispersed up to 750 °C when the heat of interaction between the support and Rh(OH)$_3$ is exothermic. The heat of interaction and the stabilization of nanoparticles with temperature are very similar for rhodium hydroxide/oxide nanoparticles supported on nanosheets derived from KCa$_2$Nb$_3$O$_{10}$ and K$_4$Nb$_6$O$_{17}$. Similar thermochemical values were obtained with nanosheets derived from RbTaO$_3$.

This is evidence that the rhodium hydroxide has a strong covalent interaction with Nb oxide and Ta oxide supports and
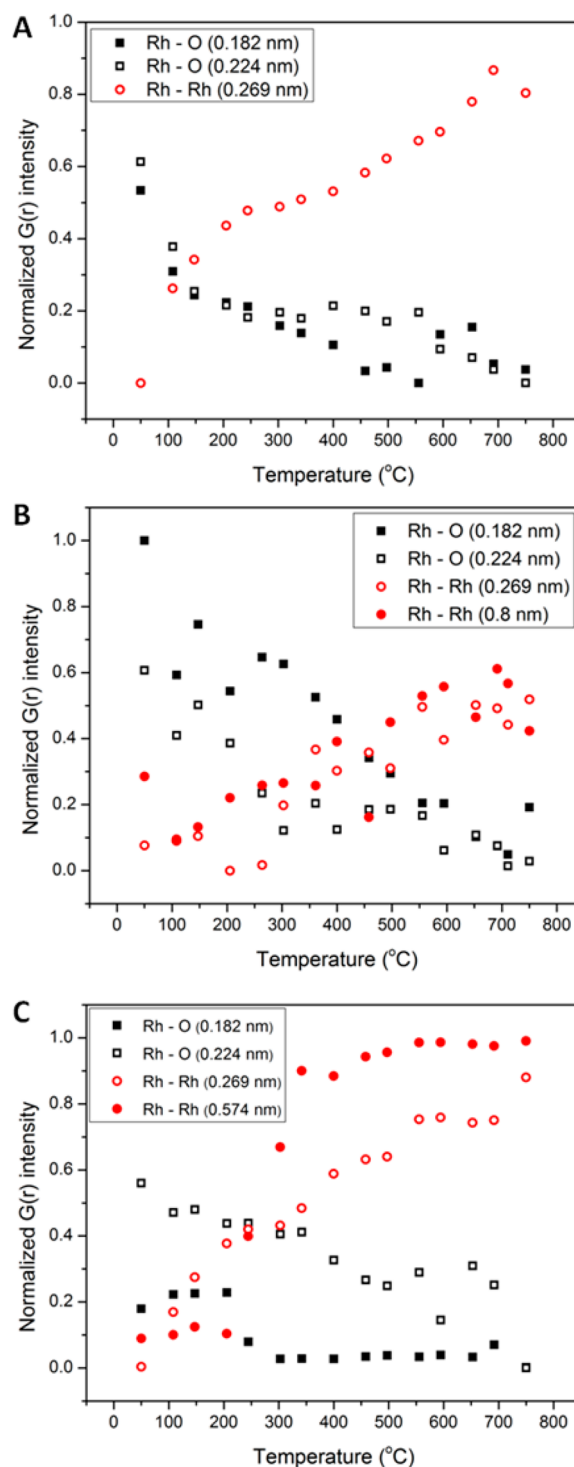

Figure 6. The normalized G(r) intensities for Rh−O and Rh−Rh correlations for rhodium hydroxide nanoparticles deposited on (A) Na-TSM, (B) KCa$_2$Nb$_3$O$_{10}$, and (C) K$_4$Nb$_6$O$_{17}$ upon heating in hydrogen.

that the structure of the support is not the major determinant of the strength of this interaction. The stabilization of Rh nanoparticles on these supports does not appear to depend on the reduction of the support, because Nb oxide and Ta oxide show similar trends. In contrast, there is an incomplete deposition of rhodium hydroxide onto high surface area SiO$_2$ and γ-Al$_2$O$_3$, and the interaction energy is endothermic. A

broad distribution of particle sizes is observed on the layered silicate, Na-TSM, and on the layered phosphate, α-ZrP.

Rh (and other late transition metal) nanoparticle catalysts on high surface area SiO_2 and γ-Al_2O_3 supports are well-known to sinter under catalytic conditions.[2,45,46] The results presented here suggest that the stability of these supported metal catalysts should correlate with the strength of interfacial bonding between the metal and the supporting oxide. ITC experiments provide a tool for directly probing the strength of this interaction under the wet chemical conditions of catalyst preparation. Because late transition metals are important for a variety of catalytic reactions, it is important to understand the trends in these interfacial interactions for a wider variety of catalytic metals and oxide supports. Experiments along these lines are currently in progress.

■ ASSOCIATED CONTENT

Ⓢ Supporting Information

Details of thermochemical calculations from ITC data, XRD patterns of layered oxide supports, HRTEM images of nanoparticles on layered oxides, TPRS data for CO oxidation, and XANES data. This material is available free of charge via the Internet at http://pubs.acs.org.

■ AUTHOR INFORMATION

Corresponding Author
tem5@psu.edu; rioux@engr.psu.edu

Notes
The authors declare no competing financial interest.

■ ACKNOWLEDGMENTS

■ REFERENCES

(1) Lee, T.; Liu, J.; Chen, N.-P.; Andres, R. P.; Janes, D. B.; Reifenberger, R. *J. Nanopart. Res.* **2000**, *2*, 345.
(2) Hansen, T. W.; DeLaRiva, A. T.; Challa, S. R.; Datye, A. K. *Acc. Chem. Res.* **2013**, *46*, 1720.
(3) Cao, A.; Lu, R.; Veser, G. *Phys. Chem. Chem. Phys.* **2010**, *12*, 13499.
(4) Hata, H.; Kobayashi, Y.; Bojan, V.; Youngblood, W. J.; Mallouk, T. E. *Nano Lett.* **2008**, *8*, 794.
(5) O'Hare, D.; Parker, K. H.; Winlove, C. P. *Med. Eng. Phys.* **2006**, *28*, 982.
(6) Cominos, V.; Hessel, V.; Hofmann, C.; Kolb, G.; Zapf, R.; Ziogas, A.; Delsman, E. R.; Schouten, J. C. *Catal. Today* **2005**, *110*, 140.
(7) Schubert, M. M.; Hackenberg, S.; van Veen, A. C.; Muhler, M.; Plzak, V.; Behm, R. J. *J. Catal.* **2001**, *197*, 113.
(8) Pestryakov, A. N.; Bogdanchikova, N. E.; Knop-Gericke, A. *Catal. Today* **2004**, *91–92*, 49.
(9) Recupero, V.; Pino, L.; Cordaro, M.; Vita, A.; Cipití, F.; Laganá, M. *Fuel Process. Technol.* **2004**, *85*, 1445.
(10) Bartholomew, C. H. *Appl. Catal., A* **1993**, *107*, 1.
(11) He, J.; Kunitake, T. *Chem. Mater.* **2004**, *16*, 2656.
(12) Wang, J.; Lu, A.-H.; Li, M.; Zhang, W.; Chen, Y.-S.; Tian, D.-X.; Li, W.-C. *ACS Nano* **2013**, *7*, 4902.
(13) Tauster, S. J. *Acc. Chem. Res.* **1987**, *20*, 389.
(14) Tauster, S. J.; Fung, S. C.; Baker, R. T. K.; Horsley, J. A. *Science* **1981**, *211*, 1121.
(15) Tauster, S. J.; Fung, S. C.; Garten, R. L. *J. Am. Chem. Soc.* **1978**, *100*, 170.
(16) Arjad, A. B.; Yarmoff, J. A. *J. Phys. Chem. C* **2012**, *116*, 23377.
(17) Belzunegui, J. P.; Sanz, J.; Rojo, J. M. *J. Am. Chem. Soc.* **1990**, *112*, 4066.
(18) Bernal, S.; Botana, F. J.; Calvino, J. J.; Lopez, C.; Perez-Omil, J. A.; Rodriguez-Izquierdo, J. M. *J. Chem. Soc., Faraday Trans.* **1996**, *92*, 2799.
(19) Fu, Q.; Wagner, T.; Olliges, S.; Carstanjen, H.-D. *J. Phys. Chem. B* **2004**, *109*, 944.
(20) Hu, Z.; Nakamura, H.; Kunimori, K.; Asano, H.; Uchijima, T. *J. Catal.* **1988**, *112*, 478.
(21) Martens, J. H. A.; Prins, R.; Zandbergen, H.; Koningsberger, D. C. *J. Phys. Chem.* **1988**, *92*, 1903.
(22) Silly, F.; Castell, M. R. *J. Phys. Chem. B* **2005**, *109*, 12316.
(23) Liu, X.; Liu, M.-H.; Luo, Y.-C.; Mou, C.-Y.; Lin, S. D.; Cheng, H.; Chen, J.-M.; Lee, J.-F.; Lin, T.-S. *J. Am. Chem. Soc.* **2012**, *134*, 10251.
(24) Campbell, C. T. *Nat. Chem.* **2012**, *4*, 597.
(25) Jarvis, E. A.; Carter, E. A. *Phys. Rev. B* **2002**, *66*, 100103.
(26) Brewer, L. *Acta Metall.* **1967**, *15*, 553.
(27) Srikrishnan, V.; Ficalora, P. J. *Metall. Trans.* **1974**, *5*, 1471.
(28) Ma, R.; Kobayashi, Y.; Youngblood, W. J.; Mallouk, T. E. *J. Mater. Chem.* **2008**, *18*, 5982.
(29) Campbell, C. T.; Starr, D. E. *J. Am. Chem. Soc.* **2002**, *124*, 9212.
(30) Farmer, J. A.; Campbell, C. T. *Science* **2010**, *329*, 933.
(31) Wiseman, T.; Williston, S.; Brandts, J. F.; Lin, L.-N. *Anal. Biochem.* **1989**, *179*, 131.
(32) Ghai, R.; Falconer, R. J.; Collins, B. M. *J. Mol. Recognit.* **2012**, *25*, 32.
(33) Gasperin, M.; Le Bihan, M. T. *J. Solid State Chem.* **1982**, *43*, 346.
(34) Kobayashi, Y.; Hata, H.; Salama, M.; Mallouk, T. E. *Nano Lett.* **2007**, *7*, 2142.
(35) Dion, M.; Ganne, M.; Tournoux, M. *Mater. Res. Bull.* **1981**, *16*, 1429.
(36) Fang, M.; Kim, C. H.; Saupe, G. B.; Kim, H.-N.; Waraksa, C. C.; Miwa, T.; Fujishima, A.; Mallouk, T. E. *Chem. Mater.* **1999**, *11*, 1526.
(37) Fukuda, K.; Nakai, I.; Ebina, Y.; Ma, R.; Sasaki, T. *Inorg. Chem.* **2007**, *46*, 4787.
(38) Kaschak, D. M.; Johnson, S. A.; Hooks, D. E.; Kim, H.-N.; Ward, M. D.; Mallouk, T. E. *J. Am. Chem. Soc.* **1998**, *120*, 10887.
(39) Chupas, P. J.; Chapman, K. W.; Jennings, G.; Lee, P. L.; Grey, C. P. *J. Am. Chem. Soc.* **2007**, *129*, 13822.
(40) Chen, Y.; Zhao, X.; Ma, H.; Ma, S.; Huang, G.; Makita, Y.; Bai, X.; Yang, X. *J. Solid State Chem.* **2008**, *181*, 1684.
(41) Hata, H.; Kobayashi, Y.; Mallouk, T. E. *Chem. Mater.* **2006**, *19*, 79.
(42) Fu, Q.; Yang, F.; Bao, X. *Acc. Chem. Res.* **2013**, *46*, 1692.

(43) Ligthart, D. A. J. M.; van Santen, R. A.; Hensen, E. J. M. *Angew. Chem., Int. Ed.* **2011**, *50*, 5306.

(44) Padeste, C.; Cant, N.; Trimm, D. *Catal. Lett.* **1994**, *28*, 301.

(45) Nagai, Y.; Hirabayashi, T.; Dohmae, K.; Takagi, N.; Minami, T.; Shinjoh, H.; Matsumoto, S. i. *J. Catal.* **2006**, *242*, 103.

(46) Shinjoh, H. *Catal. Surv. Asia* **2009**, *13*, 184.

(47) McCarty, J. G.; Malukhin, G.; Poojary, D. M.; Datye, A. K.; Xu, Q. *J. Phys. Chem. B* **2004**, *109*, 2387.

(48) Biesterbos, J. W. M.; Hornstra, J. *J. Less-Common Met.* **1973**, *30*, 121.

(49) Newton, M. A.; Dent, A. J.; Diaz-Moreno, S.; Fiddy, S. G.; Jyoti, B.; Evans, J. *Chem.—Eur. J.* **2006**, *12*, 1975.

(50) DeLaRiva, A. The sintering and stability of catalytic nanoparticles. Ph.D. Thesis, The University of New Mexico, July 2010.

(51) Ohyama, J.; Teramura, K.; Okuoka, S.-i.; Yamazoe, S.; Kato, K.; Shishido, T.; Tanaka, T. *Langmuir* **2010**, *26*, 13907.

5696

dx.doi.org/10.1021/ja412933k | *J. Am. Chem. Soc.* 2014, 136, 5687–5696